HIGH FIDELITY START-TO-END NUMERICAL PARTICLE SIMULATIONS AND PERFORMANCE STUDIES FOR LCLS-II

G. Marcus, Y. Ding, P. Emma, Z. Huang, T. O. Raubenheimer, L. Wang
SLAC, Menlo Park, CA 94025, USA
J. Qiang, M. Venturini, LBNL, Berkeley, CA 94720, USA

Abstract

High fidelity numerical particle simulations that leverage a number of accelerator and FEL codes have been used to analyze the LCLS-II FEL performance. Together, the physics models that are included in these codes have been crucial in identifying, understanding, and mitigating a number of potential hazards that can adversely affect the FEL performance, some of which are discussed in papers submitted to this conference [1, 2]. Here, we present a broad overview of the LCLS-II FEL performance, based on these start-to-end simulations, for both the soft X-ray and hard X-ray undulators including both SASE and self-seeded operational modes.

INTRODUCTION

The LCLS-II is an advanced x-ray FEL light source that consists of two independently tunable undulators capable of producing radiation covering a large spectral range that can be fed by both a CW superconducting RF (SCRF) linac or by the existing copper linac [3]. Each undulator beamline will be dedicated to the production of either hard (HXR) or soft (SXR) x-ray photons and will incorporate self-seeding [4, 5] infrastructure to produce narrow-bandwidth and longitudinally coherent FEL pulses. Addtional details regarding the baseline design can be found elsewhere [3, 6, 7].

It has been found that the relatively low electron beam energy of 4 GeV (compared to the nominal operation of LCLS) along with an extended transport distance from the end of the linac to the entrance of the undulators leaves the electron beam susceptible to a space-charge driven microbunching instability (MBI) [8–10]. This MBI manifests as large slice current and energy modulations that can potentially degrade the FEL performance. In addition, the space-charge MBI is the leading candidate responsible for the production of a self-seeded spectral 'pedestal' which is seen in both experiment [11] and in simulation [12] and is the topic of current theoretical study [2, 13].

This paper reports the results of high fidelity numerical particle simulations using the suite of codes IMPACT [14–16] and GENESIS [17]. These simulations include the effects of three-dimenstonal space charge, coherent and incoherent synchrotron radiation, RF cavity wakefields and resistive wall wakefields in the generation, acceleration and transport of the electron beam from the cathode to the undulator for three charge distributions: 20 pC, 100 pC, and 300 pC. To model the initial shot noise of the electron beam, which may act as the seed for the space-charge driven MBI, the real number of electrons were tracked from the cathode. The various charge distributions were then used to define the electron beams in GENESIS, where resistive wall wakefield effects are also included in the FEL simulations. SASE has been studied across the tuning ranges for each of the individual charge distributions for both the HXR and SXR undulators and include fully time-dependent taper optimizations. Preliminary results for self-seeding with the 100 pC electron beam will also be discussed.

ELECTRON BEAM PROPERTIES

A detailed start-to-end simulation study of the accelerator beam delivery system is reported elsewhere [1, 18]. Below, we present the electron beam longitudinal phase space (LPS) and critical slice parameters for each of the charge distributions discussed above at the entrance to the SXR undulator. The LPS of the electron beams at the entrance to the HXR undulator show less effects of MBI for reasons discussed in [18]. This sets the stage for detailed FEL simulations in the following section.

20 pC

Figure 1 shows the LPS along with various slice properties of the 20 pC electron beam that has been tracked to the SXR undulator. The core of the distribution is roughly 8 μm long,

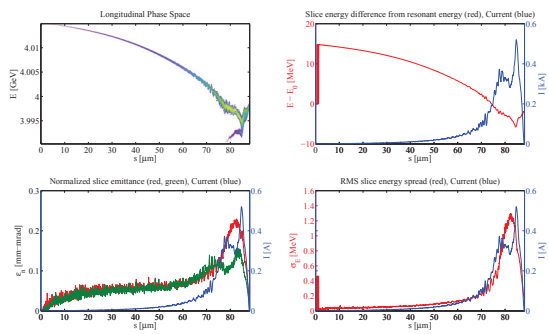

Figure 1: Slice properties of the 20 pC electron beam that has been tracked to the SXR undulator. Top left: longitudinal phase space; top right: slice energy deviation from the resonant energy (red) and current (blue); bottom left: normalized slice emittance (x-red, y-green) and current (blue); bottom right: rms slice energy spread (red) and current (blue).

is slightly chirped with the head of the beam having a lower energy, and has a $I \sim 300$ A current. The normalized slice emittance is less than $\epsilon_n \sim 0.2$ μm in both transverse planes, so while the current is rather low, the beam is sufficiently bright such that it can produce greater than 20 μJ of energy

ISBN 978-3-95450-134-2

per pulse at the high end of the tuning range in the HXR undulator (5 keV), which is important for operations. The rms slice energy spread in the core of the beam reads as greater than $\sigma_E \sim 1.2$ MeV, but is really closer to $\sigma_E \sim 0.45$ MeV if one neglects the filamentation seen in the LPS from the calculation.

100 pC

Figure 2 shows the LPS along with various slice properties of the 100 pC electron beam that has been tracked to the SXR undulator. It is obvious that the space-charge driven

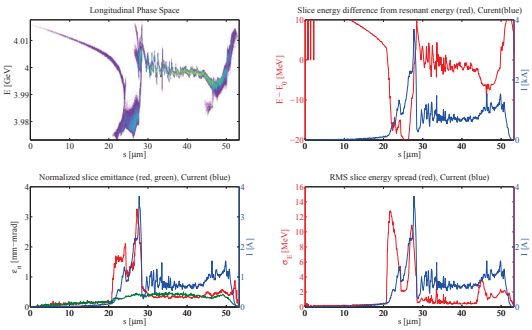

Figure 2: Slice properties of the 100 pC electron beam that has been tracked to the SXR undulator. Top left: longitudinal phase space; top right: slice energy deviation from the resonant energy (red) and current (blue); bottom left: normalized slice emittance (x-red, y-green) and current (blue); bottom right: rms slice energy spread (red) and current (blue).

MBI has severely impacted the LPS of the beam where large current and energy variations can be seen along the longitudinal profile. Nevertheless, the current in the core, which is roughly 20 μm long, is about $I \sim 750$ A. Peak to peak energy variations along the longitudinal profile can be as large as 8 MeV just after the large current spike in the tail of the beam. The normalized slice emittance is less than $\epsilon_n \sim 0.43$ μm in both transverse planes while the rms slice energy spread is roughly $\sigma_E \sim 0.55$ MeV.

300pC

Figure 3 shows the LPS along with various slice properties of the 300 pC electron beam that has been tracked to the SXR undulator. The core of this distribution, which is less impacted by the space-charge induced MBI than the 100 pC electron beam, is roughly 50 μm long and has a current of $I \sim 900$ A. The normalized slice emittance is less than $\epsilon_n \sim 0.70$ μm in both transverse planes while the rms slice energy spread is roughly $\sigma_E \sim 0.40$ MeV. While the larger transverse emittance for this charge distribution will negatively impact the performance at the high end of the tuning range of the HXR undulator, the relatively flat LPS in the core may be useful for self-seeded or externally seeded applications [12].

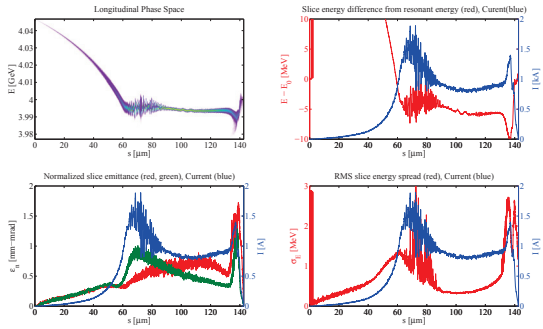

Figure 3: Slice properties of the 300 pC electron beam that has been tracked to the SXR undulator. Top left: longitudinal phase space; top right: slice energy deviation from the resonant energy (red) and current (blue); bottom left: normalized slice emittance (x-red, y-green) and current (blue); bottom right: rms slice energy spread (red) and current (blue).

SASE PERFORMANCE STUDY

Undulator Parameters

Details of the undulator layout can be found elsewhere [6, 7]. Figure 4 shows the main parameters of the HXR and SXR undulators. The undulator vacuum chamber will be

Parameter	Value SXR (HXR)	Unit
Type	Hybrid PM, planar	-
Full gap height	Variable	-
Period	39 (26)	mm
Segment length	3.4	m
Break length	1.0	m
# segments	21 (32)	-
Total length	96 (140)	m

Figure 4: LCLS-II undulator parameters.

made of aluminum and will have a rectangular cross section with a 5 mm gap height, which is used to define the resistive wall wakefield for the FEL simulations.

Tapering Optimization and Performance

The tapering scheme employed here follows the strategy laid out in [19] and is based on a three parameter optimization (z_0, ξ, d) of the final FEL pulse energy. Here the taper is given by

$$a_w(z) = a_w(z_0) \times \left[1 - c\,(z - z_0)^d\right], \qquad (1)$$

where z_0 is the taper starting location, which is typically a few power gain lengths before saturation; $c = \frac{\xi}{(L_w - z_0)^d}$, where $\xi = 1 - \frac{a_w(L_w)}{a_w(z_0)}$ is the taper ratio (the % change of the rms undulator parameter a_w over the tapered part of the

ISBN 978-3-95450-134-2

undulator) and L_w is the length of the tapered part of the undulator; and d is the taper profile order. Full time-dependent (not single slice or single frequency) taper optimizations are needed in order to capture the dynamics of SASE in the post-saturation regime accurately. The optimal taper that is nominally given by single-slice optimization scans over the three parameters listed above is more appropriate for seeded FELs. This is because particles in distinct coherence regions (SASE spikes) tend to have uncorrelated ponderomotive phases [20]. We have found that the optimal taper given by a single-slice parameter scan often produces less than half the energy that could be achieved by a full time-dependent parameter scan, which is a significant result. Figure 5 shows the result of a typical parameter scan for the 100 pC electron beam resonant at $E_\gamma = 1.5$ keV in the HXR undulator for one particular taper starting location, z_0. The taper profile order, d, is typically around 2 and the optimal taper ratio, ξ, depends on the undulator length and various electron beam and radiation properties. A summary of the LCLS-II SASE performance with post-saturation tapering can be found in Figure 6 for the charge distributions and tuning ranges that span the relevant parameter spaces. The FEL seems to be insensitive to the MBI induced energy and current modulations at all but highest photon energies in the HXR undulator, where the beam is more sensitive to slice energy spread.

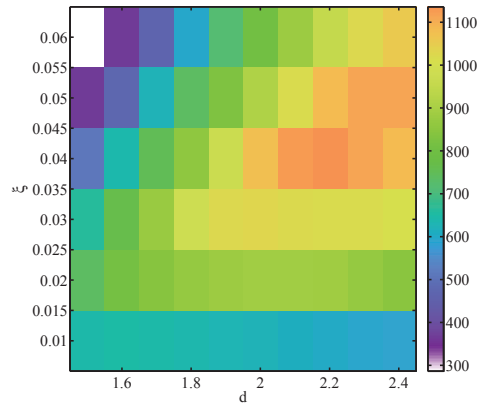

(a) Taper optimization

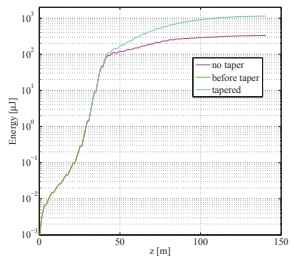

(b) Gain curve

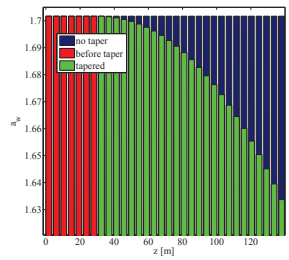

(c) Undulator taper

Figure 5: (a) taper optimization showing the energy at the end of the undulator as a function of d and ξ; (b) gain curve for the optimal taper and for the un-tapered case; (c) the taper profiles for the optimal taper and the un-tapered case.

SELF-SEEDED PERFORMANCE STUDY

Simulation Strategy

The SXR beamline will incorporate a self-seeding system (SXRSS) to produce longitudinally coherent soft x-ray free electron laser pulses. It will consist of two undulators that are separated by a monochromator and a magnetic chicane. The first undulator will consist of 7-8 independent segments while the second undulator consists of 13-14 independent segments. The monochromator design will be based on the existing LCLS SXRSS monochromator [21] with additional flexibility built in. It will have a compact footprint that is designed to allow both the chicane and monochromator to occupy the equivalent space of a single undulator segment along the strong focusing quadrupole FODO cell strongback. The resolving power is nominally specified to be $R = 15,000$, but upgrade paths to $R \sim 30,000$ are being explored.

The specification of the individual components of both the monochromator and chicane are not yet established. As such, a phenomenological approach is used to model the bandwidth reduction of the seed. The nominal monochromator design relative bandwidth ($1/R$) and overall efficiency ($\sim 5\%$) are used to specify the amplitude of a Gaussian frequency filter function. The phase of the filter function is defined through Kramers-Kronig relations such that causality

	SXR			HXR		
	250eV	750eV	1.25keV	1.5keV	3.25keV	5keV
20pC	267 (42)	239 (43)	168 (41)	206 (27)	147 (22)	25 (7)
100pC	1205 (260)	795 (135)	527 (76)	1136 (111)	469 (46)	10 (6) - (0.4)
300pC	5482 (1013)	3844 (519)	1897 (422)	2364 (300)	642 (147)	

Figure 6: LCLS-II start-to-end SASE performance study with optimized post-saturation tapering. The left column indicates the electron beam charge while the top two rows indicate either the SXR or HXR undulator and the photon energy in each undulator that was studied. The parentheses indicate the energy at saturation, which is not necessarily the energy at the end of the undulator without a post-saturation taper.

ISBN 978-3-95450-134-2

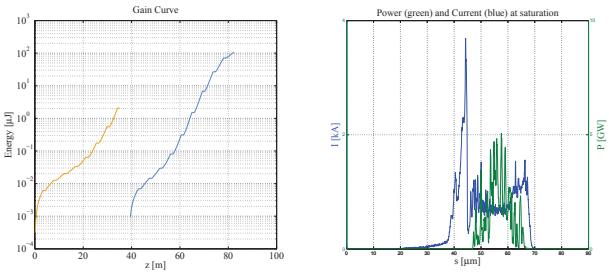

(a) Energy gain curve

(b) Power

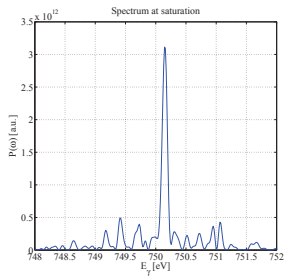

(c) Spectrum

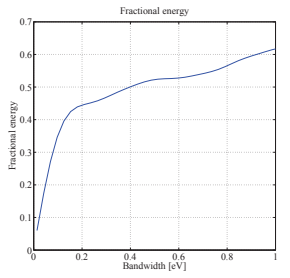

(d) Fractional energy

Figure 7: (a) Energy gain curve for the SASE undulator (orange) which generates the seed to be monochromatized and amplified downstream (blue); (b) Power (green) and current (blue) at saturation; (c) On-axis spectrum at saturation; (d) Fractional energy within a given bandwidth at saturation.

is not violated when the filter is applied to the fully three-dimensional FEL pulse exiting the seventh or eigth undulator section. The fields exiting the monochromator are then used to specify the seed into the next undulator. Diffraction through the actual monochromator setup is not modeled. This is, however, a small effect at these photon energies. In addition, a new and simple optical propagation theory has been developed to track the full three-dimensional field through the optical lattice and will be explored when the monochromator design has matured [22].

The magnetic chicane serves the dual role of compensating for the delay introduced by the monochromator and destroying any residual electron beam microbunching from the first undulator. This is modeled in a very simple way by using the dumped particle distribution and re-initializing the shotnoise.

Performance

The nominal performance for the SXRSS system using the 100 pC electron beam distribution tuned to produce $E_\gamma = 750$ eV photons is illustrated in Figure 7. The first undulator terminates the field growth well before saturation after 8 undulator sections (orange, Figure 7a). Here, the FEL energy is roughly 2 μJ while the longitudinal profile in both the spectral and temporal domain display the typical SASE spiking. The field is then frequency filtered while the electron beam shotnoise is re-initialized according to the description above. The field is amplified to saturation in a downstream undulator (blue, Figure 7a). The temporal duration at this point is roughly $\Delta T_{FWHM} \sim 36$ fs (Green, Figure 7b), which is consistent with the resolving power of $R = 15,000$ at this photon energy. Some spiking due to the fluctuating electron beam slice properties is evident. The spectrum at this point (Figure 7c) has a dominant spike with a spectral width $\Delta E_\gamma \sim 100$ meV, which is roughly twice as large as the initial bandwidth, which is defined by the monochromator bandwidth. This is a result of the longer wavelength energy and density modulations present along the LPS of the electron beam. Additionally, the higher frequency modulations produces the additional frequency content shown in the figure. These effects conspire to lower the fractional energy which is stored within the primary bandwidth of the FEL pulse, which in turn lowers the overall peak spectral brightness.

SUMMARY AND CONCLUSION

The relatively low energy of the LCLS-II electron beam and the long transport from the linac to the undulators leaves the beam susceptible to a strong space-charge driven microbunching instability, which in turn generates longitudinal variations of the electron beam slice properties. These variations may negatively impact the FEL performance. As such, high fidelity numerical particle simulations have been performed in an attempt to capture the relevant physics and to evaluate the performance of the FEL under these circumstances. Three separate charge distributions were evaluated in both the SXR and HXR undulators across the their full tuning ranges. In addition, time-dependent taper optimizations were performed in order to more accurately characterize an optimal performance. It was found that the MBI induced energy and current variations had only a small impact on the SASE FEL performance while the seeded performance showed the production of a broadband spectral 'pedestal.' Schemes to mitigate the pedestal are currently under investigation.

ACKNOWLEDGMENT

This work was supported by U.S. Department of Energy Contract No. DE-AC02-76SF00515.

ISBN 978-3-95450-134-2

REFERENCES

[1] M. Venturini *et al.*, "The microbunching instability and LCLS-II lattice design: lessons learned", in *These Proceedings: Proc. 37th Int. Free-Electron Laser Conf., Daejeon*, 2015, TUC01.

[2] Z. Zhang *et al.*, "Microbunching-induced sidebands in a seeded free-electron laser", in *These Proceedings: Proc. 37th Int. Free-Electron Laser Conf., Daejeon*, 2015, WEP084.

[3] T. Raubenheimer, "LCLS-II: Status of the CW X-ray FEL Upgrade to the LCLS Facility", in *These Proceedings: Proc. 37th Int. Free-Electron Laser Conf., Daejeon*, 2015, WEP014.

[4] J. Feldhaus *et al.*, *Opt. Comm.* **140**, 341 (1997).

[5] G. Geloni *et al.*, *Journ. Mod. Opt.* **58**, 16 (2011).

[6] T. O. Raubenheimer,"Technical Challenges of the LCLS-II", *in Proceedings: Proc. 6th Int. Part. Acc. Conf., Richmond*, 2015, WEYC1.

[7] G. Marcus, "FEL Simulation and Performance Studies for LCLS-II', *in Proceedings: Proc. 36th Int. Free-Electron Laser Conf., Basel*, 2014, TUP032.

[8] M. Borland *et al.*, *Nucl. Instrum. Methods Phys. Res. Sect. A*, **483**, 268 (2002).

[9] E. L. Saldin *et al.*, *Nucl. Instrum. Methods Phys. Res. Sect. A*, **490**, 1 (2002).

[10] Z. Huang *et al.*, *Phys. Rev. ST Accel. Beams*, **7**, 074401 (2004).

[11] D. Ratner *et al.*, *Phys. Rev. Lett.*, **114**, 054801 (2015).

[12] G. Penn *et al.*, "Effect of Microbunching on Seeding Schemes for LCLS-II", in *These Proceedings: Proc. 37th Int. Free-Electron Laser Conf., Daejeon*, 2015, WEP025.

[13] R. Lindberg, unpublished.

[14] J. Qiang *et al.*, *Phys. Rev. ST Accel. Beams*, **9**, 044204 (2006).

[15] J. Qiang *et al.*, *J. of Comp. Phys.*, **163**, 434 (2000).

[16] J. Qiang *et al.*, *Phys. Rev. ST Accel. Beams*, **12**, 100702 (2009).

[17] S. Reiche, *Nucl. Instr. Meth. Phys. Res. Sec. A* **429**, 243 (1999).

[18] J. Qiang *et al.*, "Start-to-End Simulation of the LCLS-II Beam Delivery System with Real Number of Electrons", in *These Proceedings: Proc. 37th Int. Free-Electron Laser Conf., Daejeon*, 2015, WEP070.

[19] Y. Jiao *et al.*, *Phys. Rev. ST Accel. Beams*, **15**, 050704 (2012).

[20] W. M. Fawley, *Nucl. Instr. Meth. Phys. Res. Sec. A* **483**, 537 (2002).

[21] Y. Feng *et al.*, "System Design for Self-Seeded the LCLS at Soft X-ray Energies", in *Proc. 34th Int. Free-Electron Laser Conf.*, Nara, 2012, TUoBI01.

[22] G. Marcus, *to be published.*

ISBN 978-3-95450-134-2